

Article

Enhanced Performance of Nickel–Cobalt Oxides as Selective Coatings for Flat-Plate Solar Thermal Collector Applications

Reyna Dianela Bacelis-Martínez ^{1,†}, Dallely Melissa Herrera-Zamora ^{2,†}, Manuel Ávila Santos ³, Octavio García-Valladares ², Adriana Paola Franco-Bacca ¹, Geonel Rodríguez-Gattorno ^{1,*}, and Miguel Ángel Ruiz-Gómez ^{4,*}

¹ Department of Applied Physics, CINVESTAV-IPN, Mérida 97310, Yucatán, Mexico; reyna.bacelis@cinvestav.mx (R.D.B.-M.); adriana.franco@cinvestav.mx (A.P.F.-B.)

² Instituto de Energías Renovables de la Universidad Nacional Autónoma de México (IER-UNAM), Privada Xochicalco s/n Temixco, Temixco 62580, Morelos, Mexico; dmhz@ier.unam.mx (D.M.H.-Z.); ogv@ier.unam.mx (O.G.-V.)

³ CICATA-Legaria, Instituto Politécnico Nacional, Ciudad de México 11500, Mexico; jmavilas@ipn.mx

⁴ CONAHCYT-Department of Applied Physics, CINVESTAV-IPN, Mérida 97310, Yucatán, Mexico

* Correspondence: geonelr@cinvestav.mx (G.R.-G.); miguel.ruiz@cinvestav.mx (M.Á.R.-G.)

† These authors contributed equally to this work.

Abstract: Solar thermal collectors represent a practical option to capture energy from the sun, providing low-cost domestic and industrial heating and decreasing the dependency on fossil fuels. Spinel-type metal oxides show interesting physicochemical properties and so can be used as active materials for converting solar energy to electrical, chemical, and heat energy. We report the synthesis and characterization of nickel–cobalt mixed metal oxides used as an active phase in selective paints for solar absorber coatings applied to a domestic flat collector. The nickel–cobalt mixed oxides crystallized in the cubic phase related to the spinel structure, exhibiting good thermal stability and reproducibility. These mixed oxides presented oxidation states (2+ and 3+) for both nickel and cobalt. The coatings fabricated from the selective paints based on nickel–cobalt mixed oxides showed a solar absorptance value of 94%, while for the commercial paint Solkote[®], the value was 93%. A representative coating based on the NiCo₂O₄ composition was evaluated for the first time in a domestic-type flat solar collector for water heating under real operating conditions, achieving an outstanding performance that competes with that of commercial collectors. The potential application of nickel–cobalt mixed oxides in solar collectors opens up new opportunities for future innovations and developments in functional absorber coatings.

Keywords: solar absorber coatings; solar-to-thermal energy conversion; spinel oxides



Citation: Bacelis-Martínez, R.D.; Herrera-Zamora, D.M.; Ávila Santos, M.; García-Valladares, O.; Franco-Bacca, A.P.; Rodríguez-Gattorno, G.; Ruiz-Gómez, M.Á. Enhanced Performance of Nickel–Cobalt Oxides as Selective Coatings for Flat-Plate Solar Thermal Collector Applications. *Coatings* **2023**, *13*, 1329. <https://doi.org/10.3390/coatings13081329>

Academic Editors: Yasong Sun, Mingjian He, Zhaolong Wang and Boxiang Wang

Received: 25 June 2023

Revised: 24 July 2023

Accepted: 26 July 2023

Published: 28 July 2023



Copyright: © 2023 by the authors. Licensee MDPI, Basel, Switzerland. This article is an open access article distributed under the terms and conditions of the Creative Commons Attribution (CC BY) license (<https://creativecommons.org/licenses/by/4.0/>).

1. Introduction

Because sunlight is one of the most abundant resources on earth, its use has the potential to help us in the transition toward a green economy, decreasing our dependence on fossil fuels. Nowadays, there are different possibilities for converting solar energy, such as photovoltaic and photothermal processes. The latter have attracted new interest due to their diversity in applications from hot water to industrial heating, air conditioning, and electricity production [1–6]. However, despite significant progress in solar collectors (designs, geometries, and optical features), one area that requires greater effort is the innovation in active components for coatings with higher thermal efficiency in these systems. Solar selective absorber coatings (SSACs) are a critical component for collecting solar radiation and play an essential role in these systems, where 99% of the energy is dissipated in the wavelength range from 0.3 to 2.5 μm . An ideal SSAC should be able to effectively absorb radiation and limit its infrared radiation during a temperature rise, thus maximizing the use of solar energy. Therefore, a good SSAC requires high absorption

($\alpha > 0.9$) in the solar spectrum (0.3–2.5 μm) and low thermal emittance (ϵ) in the infrared range [7–12].

Transition metal oxides with partially filled d orbitals have d–d electronic transitions that might contribute to the high absorption of incident radiation over a wide range of the solar spectrum, exhibiting near-ideal absorbing properties [10,13]. In this context, in the past few years, several studies on metal and metal oxide selective coatings used as absorbers have been reported; see Table 1. Specifically, metal oxides with a spinel-type structure possess characteristics that make them a promising material for SSAC applications, such as redox activity, high-temperature stability, and structure stability. These spinel oxides can be synthesized with different combinations of transition metals, allowing fine-tuning of the optical properties that satisfy end-user requirements with the highest efficiency and lowest cost since these materials can be prepared using simple and inexpensive methods [13–16].

In this regard, nickel–cobalt mixed spinel oxides have received special attention, being well defined by the isobaric temperature–composition diagram of the NiO–CoO–O₂ system in the air [17,18], and the solubility of nickel in Co₃O₄ reaches up to 33 mol%, causing an expansion of the elementary spinel lattice [19]. From this system, the composition NiCo₂O₄ is the most studied because it is a promising active material for different applications. It has been reported that NiCo₂O₄ shows better electrochemical properties compared to Co₃O₄ and NiO because of the simultaneous presence of redox couples (Ni²⁺/Ni³⁺ and Co²⁺/Co³⁺) associated with its crystalline structure [20–24]. Therefore, these interesting redox properties can potentially be exploited in electrochemical and thermochemical storage technologies. Also, NiCo₂O₄ has gained great attention due to its relatively low toxicity, excellent stability, and easily controllable morphology [23,25,26]. Recently, our research group reported the deposition of NiCo₂O₄ nanoparticles on a porous ZrO₂ support to evaluate the thermophysical and optical properties of the composite NiCo₂O₄@ZrO₂. The NiCo₂O₄ nanoparticles caused a strong increase in light absorbance, improving the solar thermal conversion efficiency [27]. Compositions with the formula Ni_xCo_{3–x}O₄ have been reported for exciting applications, such as thermochemical energy storage [25], solar selective absorber coatings [28], and electrocatalytic oxygen evolution [29]. Particularly, Atchuta et al. [28] reported interesting work using nickel-doped cobaltite spinel, indicating that these oxides are good candidates for high-temperature solar selective applications. Therefore, according to the achievements mentioned before, it is interesting to open up the possibility of using nickel–cobalt mixed oxides as promising materials for energy applications.

As presented in Table 1, many of the materials reported [10,28,30–39] as SSACs have not been evaluated in scale-up tests, avoiding establishing their real potential for a specific solar collection process. With this in mind, this work is focused on developing selective coatings based on spinel-type nickel–cobalt mixed oxides and evaluating their performance under operating conditions in a domestic-type flat collector for water heating. For this purpose, materials with the composition Ni_xCo_{3–x}O₄ ($x = 0.1, 0.25, 0.5, 1,$ and 1.5) were synthesized using a simple and cost-effective nitrate decomposition reaction. The obtained powders were used to formulate paints, which were further applied for the fabrication of selective coatings. An integral characterization of the powders and coatings was performed using different techniques. Finally, a representative selective coating was chosen to assemble a flat collector and evaluate its performance under realistic weather conditions.

Table 1. Summary of metals and metal oxides used as solar selective absorber coatings.

Composition	Method of Fabrication	Substrate	Solar Absorbance (α)	Thermal Emittance (ϵ)	Scale-Up Test	Year/Ref.
Ni _x Co _{3–x} O ₄	Dip-coating method	Stainless Steel	0.92	0.14	No	2019 [28]
Ni _{0.9} Fe _{0.1} Co ₂ O _y	Sol-gel, spraying	Stainless Steel	0.93	0.11	No	2021 [30]
Cu _{0.5} Cr _{1.1} Mn _{1.4} O ₄	Hydrothermal technique, co-precipitation, spray coating	Haynes 230	0.97	0.88	No	2019 [31]

Table 1. Cont.

Composition	Method of Fabrication	Substrate	Solar Absorptance (α)	Thermal Emittance (ϵ)	Scale-Up Test	Year/Ref.
Co–Cr, SiO ₂	Electroplating, dip coating	Stainless Steel	0.96	0.12	No	2022 [32]
Nickel/black Cobalt	Electrodeposition	Stainless Steel	0.95	0.07	Yes	2020 [33]
CuCr _x Mn _{2-x} O ₄	Sol-gel combustion/spray-coating technique	Aluminum	0.92–0.93	0.22–0.31	No	2012 [34]
CuMnNiO _x , SiO ₂ and MgF ₂	Sol-gel, solvothermal technique, dip coating	Stainless Steel	0.94	0.14	No	2022 [10]
Co:Ni:Mn = 2:1:1	Dip coating	Stainless Steel	0.91	0.13	No	2023 [35]
Nickel–Black Nickel	Electrodeposition	Copper	0.90	0.08	Yes	2019 [36]
Cr/Cr ₂ O ₃	Electrodeposition	Stainless Steel	0.90	NA	No	2018 [37]
Black Nickel	Electrodeposition	Copper	0.85	0.11	Yes	2022 [38]
C/Ni/NiO	Sol-gel, spin coating	Copper	0.80	0.11	No	2019 [39]

NA: no available information.

2. Materials and Methods

2.1. Synthesis of Powder Metal Oxides

Five compositions with the formula Ni_xCo_{3-x}O₄ (where $x = 0.1, 0.25, 0.5, 1,$ and 1.5) and the simple oxides Co₃O₄ and NiO used as a reference were synthesized using a simple nitrate decomposition reaction. For this, an appropriate molar amount of nickel nitrate (Ni(NO₃)₂ · 6H₂O) and/or cobalt nitrate (Co(NO₃)₂ · 6H₂O) was dissolved in 15 mL of deionized water (18.2 MΩ·cm). Next, the respective solutions were put in a crucible and heated at 250 °C on a hot plate for 2 h until complete evaporation of water. The obtained powders were homogenized using an agate mortar. Next, they were placed in a ceramic crucible and thermally treated at 500 °C for 1 h in an air atmosphere with a heating rate of 2 °C/min. All metal oxide powders were homogenized for further characterization.

2.2. Characterization of Powder Metal Oxides

The resulting powders were characterized using powder X-Ray diffraction in a Bruker D8 Advance Eco diffractometer (Bruker, Billerica, MA, USA) using the wavelength Cu-K $\alpha = 1.5418$ Å. The measurements were carried out at room temperature from 30° to 70° in 2 θ , at a step size of 0.02°, a step time of 1.5 s, and 40 kV and 25 mA. The obtained XRD patterns were compared with the PDF-2 database of the International Centre for Diffraction Data to identify crystalline phases. Raman spectroscopy measurements were performed at 25 °C, and the spectra were acquired from an average of 10 exposures with 2 s acquisition and a resolution of 2.7 to 4.2 cm⁻¹. The excitation wavelength corresponds to a 532 nm laser, which was focused to an estimated spot size of 2.1 μ m using a 10 \times /0.4 bd objective lens (Thermo Scientific, Waltham, MA, USA). The intensity of the laser was controlled from 0.1 to 10 mW. Oxidation states and elemental quantification were examined using the X-Ray photoelectron spectroscopy (XPS) technique with a K-Alpha (Thermo Scientific, Waltham, MA, USA) spectrometer with monochromatized Al K α radiation (1486.6 eV) at 12 kV and 40 W. The analyzed area was 400 μ m² using a relative incident angle of 30°. Before analysis, the surface of the samples was cleaned using argon erosion (30 s at 3 kV and 30 W). Survey spectra were obtained from 0 to 1350 eV (1 eV/step and 100 eV pass energy), whereas for high-resolution spectra, 0.1 eV/step and 50 eV pass energy were used. The binding energies were referenced to adventitious carbon (C 1s) at 284.8 eV. The microstructural and chemical compositions were analyzed using scanning electron microscopy and energy-dispersive X-ray spectroscopy (SEM-EDS) with a JEOL

JSM-7600F microscope (JEOL, Tokyo, Japan) and an X-Max Oxford Instruments detector (Oxford Instruments plc, Oxford, UK), respectively. For analysis, a small amount of the sample was dispersed directly onto carbon tape placed on an aluminum sample holder. Additionally, thermogravimetric analysis was carried out using TA Instruments-Discovery equipment (TA Instruments, New Castle, DE, USA). For measurements, ~20 mg of the sample was placed in a platinum crucible, and the analysis consisted of three continuous heating/cooling cycles using a ramp rate of 5 °C/min in an air atmosphere (20 mL/min). The cycles were carried out as follows: (1) from 30 to 1000 °C and from 1000 to 100 °C, (2) from 100 to 1000 °C and from 1000 to 500 °C, and (3) from 500 to 1000 °C and from 1000 to 500 °C, without a dwelling step in any cycle.

2.3. Use of Powders to Formulate Selective Paints

The obtained powders ($\text{Ni}_x\text{Co}_{3-x}\text{O}_4$, Co_3O_4 , and NiO) were used to formulate the respective paints. Although it is not possible to specify details due to the patent application, the general procedure is as follows: A specific amount of each metal oxide powder was dispersed separately with a portion of xylene in the presence of a polyester resin to obtain a typical “alkyd paint”. Next, the mixture was stirred for 30 min at 400 rpm and subsequently sonicated for 20 min. The obtained selective paints were stored for further use.

2.4. Application of Selective Paints

Recycled aluminum plates (25 cm²) were used as substrates. First, they were cleaned using 320, 600, and 2000 grit sandpaper to smooth the surface, rinsed with water, and then polished with alumina paste (1 to 0.3 μm). Later, each one of the formulated paints was applied with a brush to the cleaned plates (two sets). One set of the brush-painted plates was left to dry for 24 h without any treatment, while the other one was thermally treated at 200 °C for 24 h. Both sets of brush-painted plates were analyzed using UV–VIS–NIR–FTIR to determine their optical properties (see details later) and also characterized using other physicochemical techniques. To compare the optical properties, a set of brush-painted plates using the commercial paint Solkote[®] (SOLEC-Solar Energy Corporation, Ewing, NJ, USA) was also prepared following the described procedure.

2.5. Optical Characterization

Reflectance spectra for the synthesized powders, brush-painted aluminum plates, and spray-painted aluminum fins (see Section 2.7) were obtained in the range of 0.3 to 2.5 μm using a UV–VIS spectrometer (Avantes, model AVASpec2048, Avantes BV, Apeldoorn, The Netherlands) and an infrared spectrometer (Avantes, model AvaSpec-NIR256-2.5, Avantes BV, Apeldoorn, The Netherlands), both with an integrating sphere (Avantes, model 50-LS-HAL, Avantes BV, Apeldoorn, The Netherlands). For the UV–VIS–NIR measurements, the white reflective tile AVANTES WS-2 was obtained as a reference, consisting of a white, diffuse, and high-quality material based on PTFE, which reflects 98 % of light in the wavelength range of 350–1800 nm and more than 92 % from 250 to 2500 nm. Reflectance was measured as full hemispheric under normal illumination. The reflectance spectra in the range of 2.5 to 15 μm were obtained with an FTIR spectrometer (Perkin Elmer, Frontier NIR/MIR model, Perkin Elmer, Waltham, MA, USA), also equipped with an integrating sphere IntegratIR model (PIKE Technologies, Madison, WI, USA), using the gold standard as the reference. Solar absorption was prolonged by weighting the reflectance spectrum against the ASTM G173-0329 solar radiation spectrum, using Equation (1), while thermal emission was calculated using $T = 100$ °C and Equation (2). To determine the thermal emittance, the reflection of the coating was measured by weighting the reflection spectrum against black-body radiation at 100 °C. However, the spectra are often extrapolated to 50 μm, leading to lower values for the thermal emission upon integration with the black-body radiation curve. Based on the higher uncertainty inherent in the thermal emission values, it was preferred to report the values obtained directly from the experiments [33].

$$\alpha = \frac{\int_{0.3}^{2.5} I_{\text{SUN}}(\lambda) \times [1 - R(\lambda)] d\lambda}{\int_{0.3}^{2.5} I_{\text{SUN}}(\lambda)} \quad (1)$$

$$\varepsilon = \frac{\int_{2.5}^{15} I_{\text{BB}}(\lambda) \times [1 - R(\lambda)] d\lambda}{\int_{2.5}^{15} I_{\text{BB}}(\lambda)} \quad (2)$$

where α is the solar absorptance, I_{SUN} is the solar irradiance spectrum, $R(\lambda)$ is the wavelength-dependent reflectance, ε is the thermal emittance, and I_{BB} is the black-body radiation as a function of wavelength and temperature is given by $I_{\text{BB}}(\lambda, T) = c_1 / \left\{ \lambda^5 \left[e^{\left(\frac{c_2}{\lambda T} \right)} - 1 \right] \right\}$ with $c_1 = 3.743 \times 10^{-16} \text{ W m}^2$ and $c_2 = 1.4387 \times 10^{-2} \text{ m K}$, which are constants related to Planck's law.

2.6. Contact Angle Measurements

The two sets of brush-painted plates were evaluated to define their hydrophilicity. The affinity to water was determined by measuring the contact angle between deionized water droplets (10 μL) and each one of the brush-painted plates. Images were taken with a Dino-Lite Digital Microscope (Dino-Lite, Torrance, CA, USA), while the contact angle was estimated by processing the images using ImageJ software with the appropriate algorithm.

2.7. Scale-Up

For scale-up evaluation, the stoichiometry NiCo_2O_4 composition was chosen as a representative among all prepared oxides. The principal idea was to determine the performance of this material under real operating conditions in a domestic flat-plate solar collector. For this, the formulated NiCo_2O_4 -based selective paint was deposited onto six recycled aluminum fins (1.4 m \times 0.8 m each) using a spraying gun at a distance of 30 cm, with air as a carrier gas, operating at 50 PSI. The six spray-painted fins were used to assemble the solar collector, and the results were analyzed according to the NMX-ES-004-NORMEX-2010 standard. To facilitate all measurements, the tests were carried out on the platform of the company I + D + I Solar S.A. de C.V., which is located in Xochitepec, Morelos, Mexico (latitude: 18.7808° N, longitude: -99.2316° E, and altitude: 1108 m.a.s.l.). The tests were performed from 25 to 29 May 2022. The spray-painted fins were connected in parallel, with a valve to regulate the flow in each of them in a collector with a polyurethane bottom, a polycarbonate cover, "Pintro" sheet sides, and frames. The collector had an opening area of 1.5 m² and a capacity of 150 L. The solar irradiance, ambient temperature, and temperatures at the entrance and exit of the collector were recorded and compared with the commercial HVA collector of the company M3dulo Solar S.A. de C.V, Cuernavaca, M3xico. Figure 1 shows the general procedure conducted from the synthesis of the metal oxides up to the potential application as a solar collector.

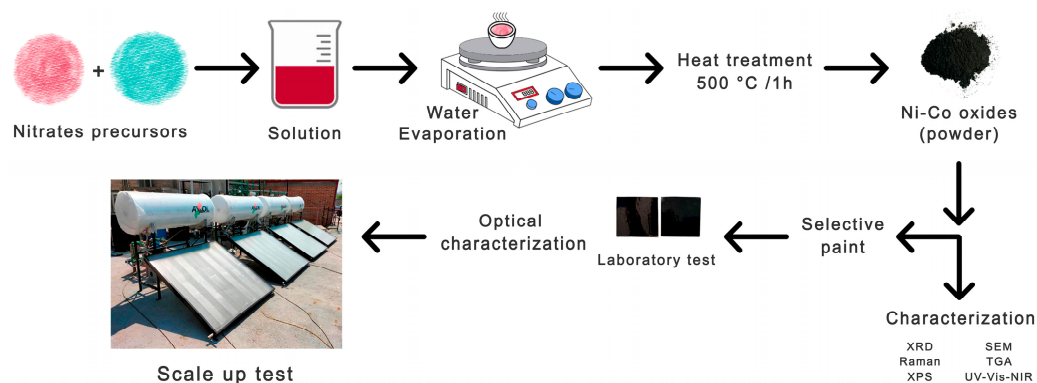


Figure 1. Schematic overview depicting the procedure for preparation of selective paints from $\text{Ni}_x\text{Co}_{2-x}\text{O}_4$ powders and their application to develop a flat solar collector.

3. Results and Discussion

3.1. Physicochemical Analysis of Synthesized Powders

Figure S1 shows photographs of all synthesized powders calcined at 500 °C for 1 h. As can be seen, Co_3O_4 and $\text{Ni}_x\text{Co}_{3-x}\text{O}_4$ samples were black in color, whereas the NiO sample was dark green. Figure 2a shows the XRD patterns obtained for these powders. The Co_3O_4 sample presented a set of peaks related to the crystal planes (220), (311), (400), (422), (511), and (440) of the cubic phase (space group Fd-3m #227, JCPDS 01-076-1802), while the patterns of $\text{Ni}_x\text{Co}_{3-x}\text{O}_4$ samples with $x = 0.1, 0.25,$ and 0.5 were similar to that of Co_3O_4 , indicating that there is no important modification of the pristine Co_3O_4 crystalline structure due to the substitution with a low amount of nickel. Nevertheless, for a nickel content of 0.25 and 0.5, a slight shift toward lower angle values was observed, suggesting an expansion of the cell volume. The samples with $x = 1.0$ and 1.5 showed the presence of NiCo_2O_4 (space group Fd-3m #227, JCPDS 01-073-1702) and NiO (space group Fm-3m #225, JCPDS 00-047-1049) phases, with the presence of NiO being more evident for the material with $x = 1.5$, in good agreement with the excess of nickel used for this composition [17–19]. It has been reported for NiCo_2O_4 ($x = 1$) that its stability is strongly affected by preparation conditions and thermal treatment [25,28,40]. For example, Portilla-Nieto et al. [25] observed the presence of a secondary phase in the material synthesized using the sol–gel method following Pechini’s route and calcined in air at 400 °C for 10 h, whereas Atchuta et al. [28] reported the presence of an additional minor phase in the material obtained using the wet-chemical method and annealed at 500 °C for 1 h. It is important to note that NiCo_2O_4 and Co_3O_4 are isostructural and that the ionic radii of nickel and cobalt are similar [41]. The JCPDS cards used for identification of Co_3O_4 and NiCo_2O_4 phases correspond to isostructural materials where the nickel atom partially occupies the same crystallographic sites as the cobalt atom, while the synthesized NiO sample is obtained as a single phase showing reflection related to the planes (111), (200), and (220) of the cubic structure (space group Fm-3m #225, JCPDS 00-047-1049).

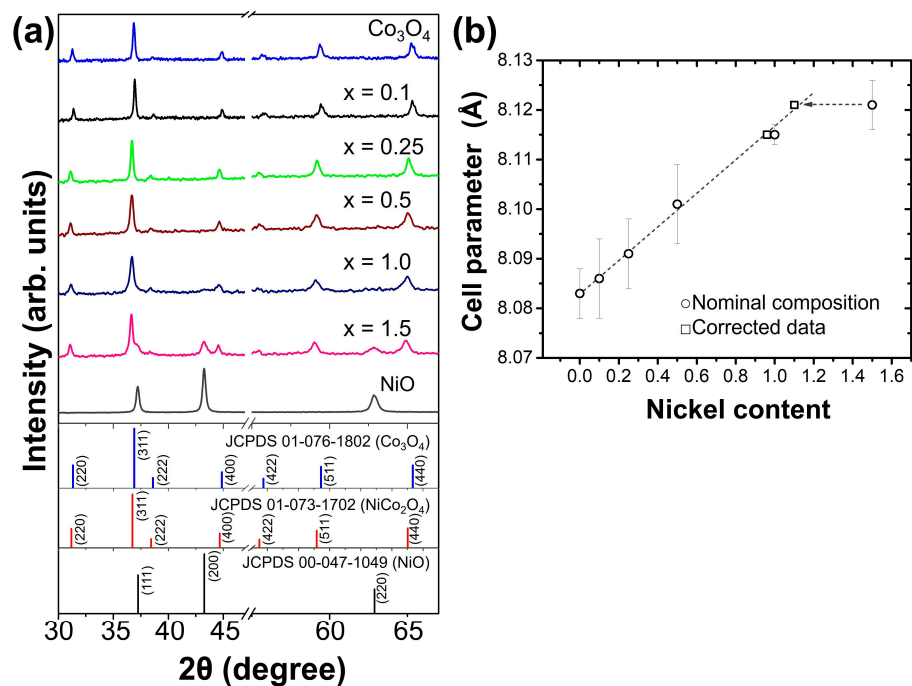


Figure 2. (a) XRD diffractograms for the $\text{Ni}_x\text{Co}_{3-x}\text{O}_4$ materials and the reference oxides Co_3O_4 and NiO and (b) variation of the cell parameter as a function of the nickel content of the $\text{Ni}_x\text{Co}_{3-x}\text{O}_4$ materials.

To confirm the identified crystalline phases, a profile fitting was made to all XRD patterns using the Le Bail method [42] implemented in the FullProf program [43]. The Le Bail profile fitting confirmed the presence of all identified phases; see Figures S2–S8.

Additionally, Rietveld refinement was performed for those samples with a mixture of crystalline phases to determine their percentage. The results showed that for the sample with $x = 1.0$, there was a phase percentage of 96.1% for NiCo_2O_4 and 3.9% for NiO (Figure S6), while for the sample with $x = 1.5$, the percentage was 73.3% for NiCo_2O_4 and 26.7% for NiO (Figure S7). Also, from the Le Bail profile fitting, the cell parameter was refined and plotted versus the nickel content, showing a tendency that clearly follows Vegard's law; see Figure 2b. The cell parameters ranged from 8.083 Å (Co_3O_4) to 8.121 Å ($x = 1.5$), and they are in good agreement with previous reports [29,40]. Those nominal compositions that deviated from Vegard's law were corrected using the phase percentages previously calculated; after correction, the values followed the linear behavior expected for the rule of mixtures.

Raman spectroscopy was also used for structural identification analysis. Figure 3 shows the obtained spectra, with Co_3O_4 and $\text{Ni}_x\text{Co}_{3-x}\text{O}_4$ ($x = 0.1, 0.25, 0.5$) samples presenting well-defined peaks at about 478, 523, 615, and 682 cm^{-1} ascribed to the Raman active vibrations modes $E_g + F_{2g} + F_{2g} + A_{1g}$, respectively, reported for Co_3O_4 [44,45]. In these samples, the peak positions shifted to high wavenumbers for the $\text{Ni}_x\text{Co}_{3-x}\text{O}_4$ materials compared to Co_3O_4 ; for example, the most intense peak varied from 682 cm^{-1} in Co_3O_4 to 706 cm^{-1} in $\text{Ni}_{0.5}\text{Co}_{2.5}\text{O}_4$. As demonstrated by the XRD analysis, there was no important modification of the pristine Co_3O_4 crystalline structure by substituting with a low amount of nickel (0.1, 0.25, and 0.5). However, the effect of the Raman shift might suggest a change in the particle size and agglomeration state. In contrast, the NiCo_2O_4 sample exhibited a peak at 698 cm^{-1} , while the peaks in the range from 470 to 620 cm^{-1} were not well defined; they could be an effect of the transition from normal-spinel Co_3O_4 to inverse-spinel NiCo_2O_4 [46,47]. The $\text{Ni}_{1.5}\text{Co}_{1.5}\text{O}_4$ sample showed two broad peaks similar to the NiO sample, at 510 and 1100 cm^{-1} [48,49].

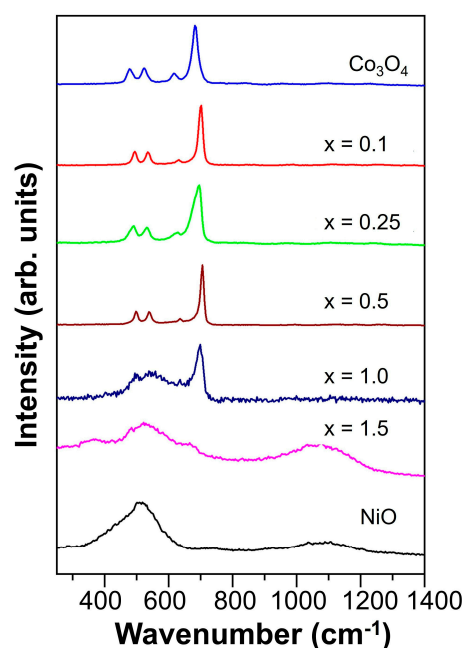


Figure 3. Raman spectra for the $\text{Ni}_x\text{Co}_{3-x}\text{O}_4$ materials and the reference oxides Co_3O_4 and NiO .

The elemental composition was determined using EDS analysis, finding only the presence of cobalt, nickel, and oxygen. Considering the theoretical atomic proportion for Co_3O_4 and NiO , Table 2 indicates that the results for all oxides had a deviation of ± 2.5 at.% as the maximum compared to the theoretical value, except for $\text{Ni}_{1.5}\text{Co}_{1.5}\text{O}_4$ and NiO oxides that had a higher deviation. In this last case, the higher deviation can be related to the possible presence of two oxidation states of nickel in NiO as well as a mixture of phases

in $\text{Ni}_{1.5}\text{Co}_{1.5}\text{O}_4$. At the same time, the EDS mapping analysis (see Figure S9) revealed a homogeneous distribution of cobalt, nickel, and oxygen in all the synthesized samples.

Table 2. Elemental composition by EDS analysis of all synthesized metal oxides.

At. %	Co_3O_4	$\text{Ni}_{0.1}\text{Co}_{2.9}\text{O}_4$	$\text{Ni}_{0.25}\text{Co}_{2.75}\text{O}_4$	$\text{Ni}_{0.5}\text{Co}_{2.5}\text{O}_4$	NiCo_2O_4	$\text{Ni}_{1.5}\text{Co}_{1.5}\text{O}_4$	NiO
Co	41.16	43.38	36.84	35.12	28.53	24.77	0
Ni	0	Not detected	3.61	7.27	15.82	27.48	44.58
O	58.84	56.62	59.55	57.61	55.65	47.75	55.42

Both transition metals (nickel and cobalt) have the ability to exhibit mixed oxidation states that significantly modulate the properties of these mixed oxides; hence, the characterization with XPS analysis is essential. Figure 4 shows the deconvoluted high-resolution XPS spectra of all oxides. Figure 4a presents the Co 2p_{3/2} region, in which all samples showed peaks centered at ~779.2 and at ~780.9 eV that are related to Co^{3+} and Co^{2+} , respectively, indicating the presence of both oxidation states. In the Ni 2p_{3/2} region presented in Figure 4b, the spectra indicate that all samples contained the mixed oxidation states for nickel due to the presence of peaks centered at ~853.9 and ~856.5 eV, which are assigned to Ni^{2+} and Ni^{3+} , respectively. Based on the thermal treatment applied and the dark-green color of the synthesized NiO sample (see Figure S1), which contrasts with the pale-green color of the stoichiometric NiO, it can be concluded that the synthesized NiO sample contains both Ni^{2+} and Ni^{3+} oxidation states, while the spectra of the O 1s region in Figure 4c are also similar for all samples, and the peaks can be assigned to lattice oxygen in metal oxides at ~529.3 eV and the presence of surface hydroxyls at ~531.1 eV [50].

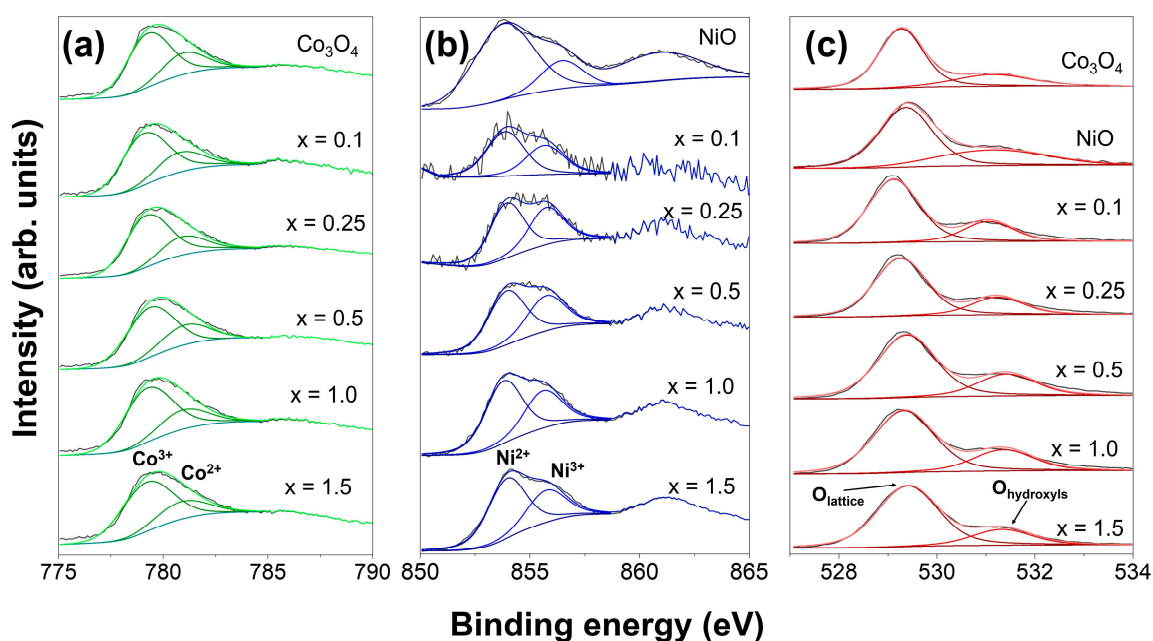


Figure 4. Deconvoluted high-resolution spectra in the region of (a) Co 2p, (b) Ni 2p, and (c) O 1s for Co_3O_4 , NiO, and $\text{Ni}_x\text{Co}_{3-x}\text{O}_4$.

Figure 5 shows the quantitative results of the oxidation states of cobalt and nickel in $\text{Ni}_x\text{Co}_{3-x}\text{O}_4$ oxides derived from the analyses shown in Figure 4. As expected, according to the formula $\text{Ni}_x\text{Co}_{3-x}\text{O}_4$, the results agree with the fact that the content of cobalt decreases and the content of nickel increases. Besides, the proportion of $\text{Co}^{3+}/\text{Co}^{2+}$ was maintained between 2.5 and 2.8, being the highest for NiCo_2O_4 and $\text{Ni}_{1.5}\text{Co}_{1.5}\text{O}_4$ samples, while the proportion of $\text{Ni}^{2+}/\text{Ni}^{3+}$ ranged between 1.5 and 1.8, where the highest predominance of

Ni^{2+} was observed for the $\text{Ni}_{1.5}\text{Co}_{1.5}\text{O}_4$ sample. The atomic percentage of surface oxygen (lattice and hydroxyls) was similar in all samples; see Figure S10.

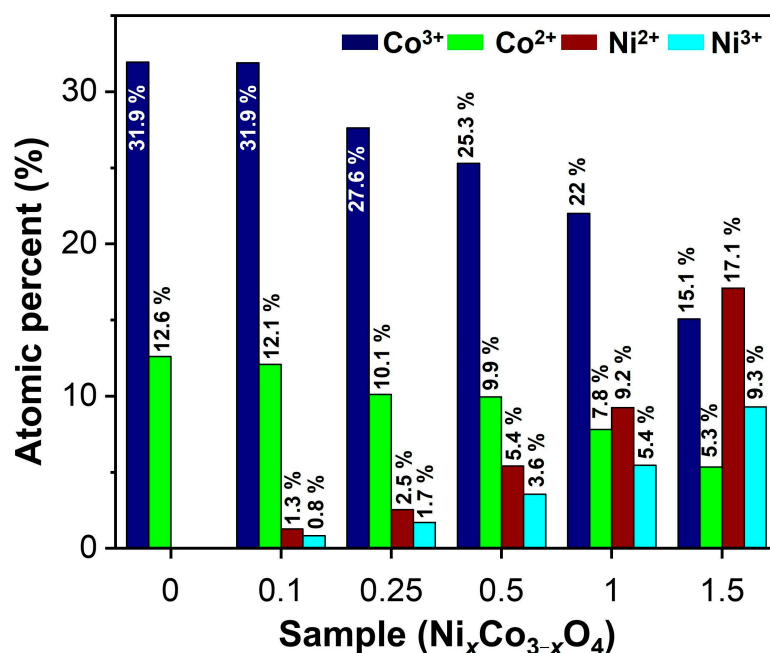


Figure 5. Quantitative analysis of the oxidation states for $\text{Ni}_x\text{Co}_{3-x}\text{O}_4$ samples.

Representative SEM images of Co_3O_4 and selected $\text{Ni}_x\text{Co}_{3-x}\text{O}_4$ materials are depicted in Figure 6. In general, all the samples (see also Figure S11) showed a similar morphology and particle size, with particles of ~ 100 nm forming agglomerates. An important effect of the composition variation on the microstructure was not appreciated. Homogeneity in the particle size distribution allowed high dispersibility of the powders during paint preparation.

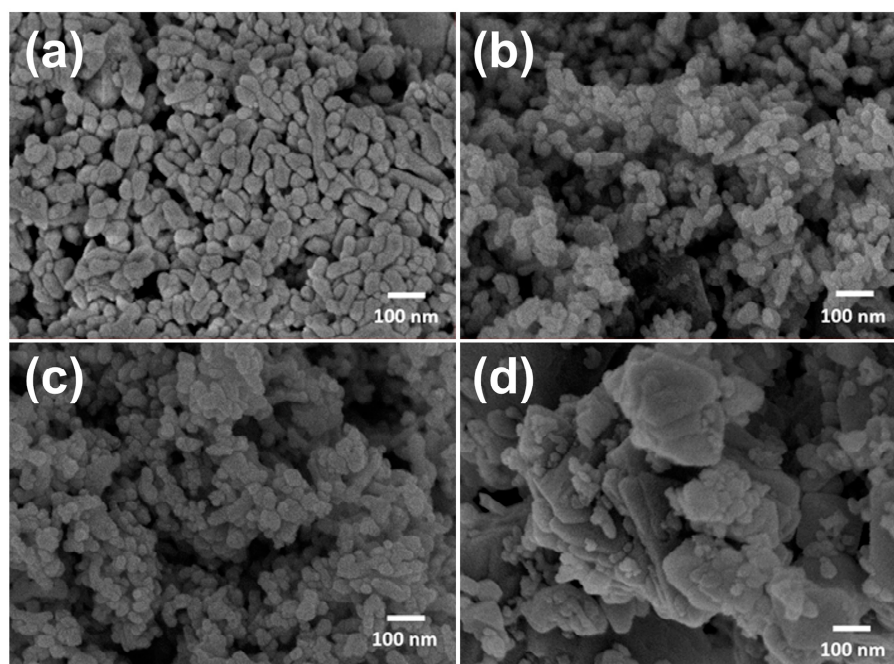


Figure 6. Representative SEM micrographs of selected samples: (a) Co_3O_4 , (b) $\text{Ni}_{0.25}\text{Co}_{2.75}\text{O}_4$, (c) NiCo_2O_4 , and (d) NiO .

Figure 7 shows the results of the typical thermogravimetry curves of Co_3O_4 and three of the $\text{Ni}_x\text{Co}_{3-x}\text{O}_4$ samples. According to the presented results, the Co_3O_4 sample depicted an onset of reduction temperature at $\sim 890^\circ\text{C}$, with a weight loss of 6.6%, in excellent agreement with the theoretical limit expected for the release of oxygen according to Equation (3) [51–53].

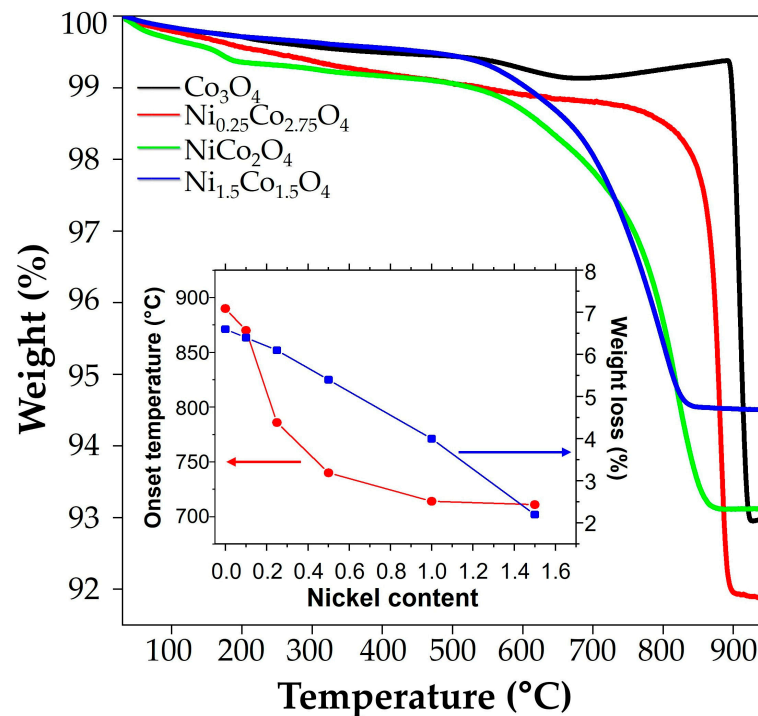
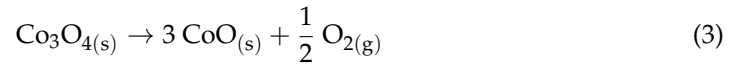


Figure 7. Thermogravimetric analysis of Co_3O_4 and $\text{Ni}_x\text{Co}_{3-x}\text{O}_4$ with $x = 0.25, 1.0,$ and 1.5 . The inset plot summarizes the results of onset temperature and weight loss for all samples.

This indicates that Co_3O_4 has been fully reduced at this step and is stable below that temperature. On cooling, Co_3O_4 recovered its weight via its re-oxidation reaction, exhibiting excellent stability and reproducibility during several cycles (see Figure S3). The samples with $\text{Ni} = 0.1, 0.25,$ and 0.5 showed similar reversible behavior, exhibiting good thermal cyclability and weight recovery. Samples with the highest Ni content showed less loss of oxygen despite their reversible weight loss at the slightest lowering of temperature (710°C). The inset in Figure 7 depicts the values of the onset of the reduction temperature and the percentage of weight loss obtained from the heating–cooling (reduction–oxidation) cycles presented in Figure S12.

Table 3 shows the solar absorptance values for all synthesized powders. All the nickel–cobalt mixed oxides exhibited slightly higher values compared to pristine Co_3O_4 . It is well documented that increasing the concentration of nickel induces the improvement of optoelectronic properties by enhancing the metallic character of this system, with a corresponding reduction in the electronic gap [54]. These results suggest the potential of these oxides as absorbers for applications related to solar capturing. When measuring optical properties in bare powders, not only should the diffuse reflections be considered, but also other kinds of them that do not follow Lambert’s law and affect the intensity of the studied peaks, producing a decrease in some properties, such as solar absorptance, compared to that obtained from solar coatings, where there is a better grain distribution on the surface [55].

Table 3. Solar absorptance values obtained for the synthesized powders.

Sample	α (%)
Co ₃ O ₄	84 ± 1
Ni _{0.1} Co _{2.9} O ₄	85 ± 1
Ni _{0.25} Co _{2.75} O ₄	86 ± 1
Ni _{0.5} Co _{2.5} O ₄	87 ± 1
NiCo ₂ O ₄	86 ± 1
Ni _{1.5} Co _{1.5} O ₄	87 ± 1
NiO	78 ± 1

3.2. Evaluation of Selective Paints

Figure 8 shows the UV–VIS–NIR spectra obtained for the brush-painted aluminum plates. Co₃O₄ and NiO paints showed the characteristic optical response of their nature [15,28,33,56–58], with the Ni_xCo_{3–x}O₄ paints having similar optical properties as those reported for NiCo₂O₄ [24,27]. It can be seen that thermal treatment (200 °C for 24 h) provoked slight changes in the intensity of some peaks in Co₃O₄ and NiO paints, while it did not affect the Ni_xCo_{3–x}O₄ paints, because the reflectance curves for both sets were similar. Some of the peaks observed in the far-infrared range (2–15 μm) could be related to the polymeric resin used to make the paints (see Figure S13). In general, the reflectance spectra obtained for our samples (from 300 to 2400 nm) correlate well with those reported [28], although a possible effect due to differences in the used substrate and the thickness of the coatings should be considered for a more specific comparison.

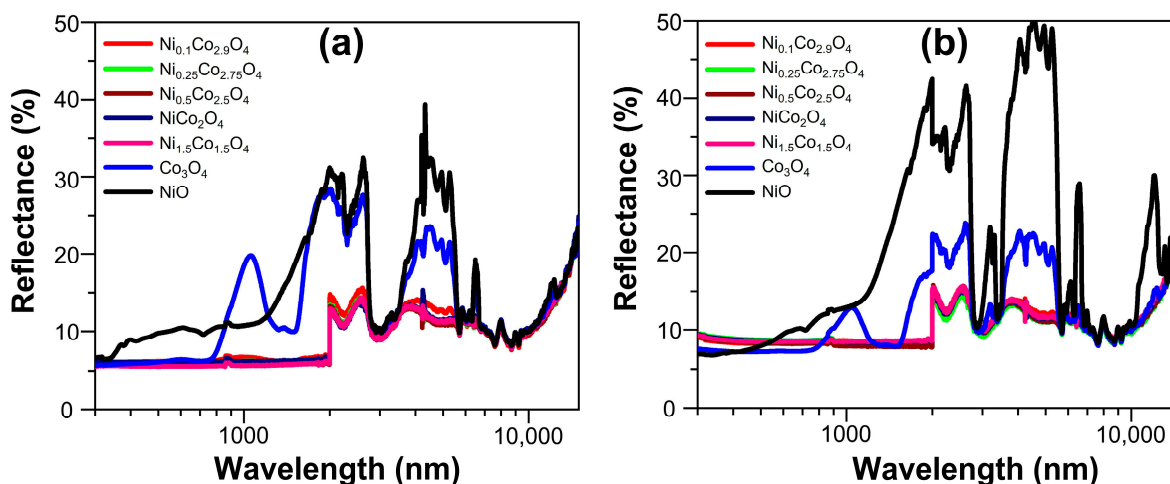


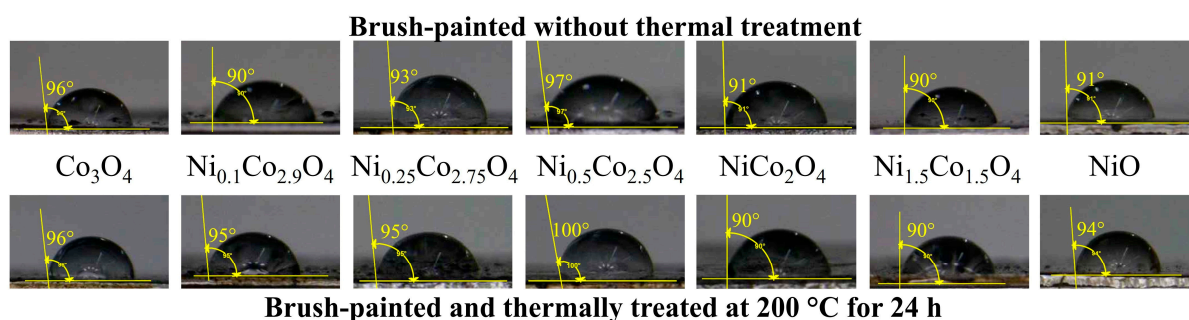
Figure 8. Reflectance spectra for two sets of brush-painted aluminum plates using the different metal-oxide-based selective paints: (a) without thermal treatment and (b) with thermal treatment at 200 °C for 24 h.

Table 4 shows the solar absorptance and thermal emittance values for brush-painted aluminum plates using the different metal-oxide-based selective paints; these values were similar, indicating good thermal stability. In particular, the brush-painted aluminum plates using the Ni_xCo_{3–x}O₄ paints had values of $\alpha \approx 94\%$ and $\epsilon \approx 88\%$, and after thermal treatment, the values of α decreased slightly and ϵ was maintained. In the case of the brush-painted aluminum plates using the commercial paint Solkote[®], see Figure S14, the obtained values were $\alpha \approx 93\%$ and $\epsilon \approx 63\%$. So, the Ni_xCo_{3–x}O₄ paints compete well in terms of α , while it would be important to consider a reformulation to decrease the ϵ value. This fact opens up the possibility for the potential use of paints based on nickel–cobalt mixed oxides to prepare selective coatings for solar capture processes, such as heating water for domestic use. Furthermore, nickel–cobalt mixed oxide formulations could be more accessible in economic terms compared to commercial paints.

Table 4. Solar absorptance and thermal emittance values for brush-painted aluminum plates using the different metal-oxide-based selective paints.

Sample	Brush-Painted without Thermal Treatment		Brush-Painted and Thermally Treated at 200 °C for 24 h	
	α (%)	ϵ (%)	α (%)	ϵ (%)
Co_3O_4	93	87	92	87
$\text{Ni}_{0.1}\text{Co}_{2.9}\text{O}_4$	94	88	92	88
$\text{Ni}_{0.25}\text{Co}_{2.75}\text{O}_4$	94	88	91	88
$\text{Ni}_{0.5}\text{Co}_{2.5}\text{O}_4$	94	88	92	88
NiCo_2O_4	94	88	91	88
$\text{Ni}_{1.5}\text{Co}_{1.5}\text{O}_4$	94	88	91	88
NiO	90	86	90	82

In contrast, all the brush-painted aluminum plates were found to be hydrophobic; see Figure 9. The contact angle values were $\geq 90^\circ$ for all brush-painted aluminum plates, without thermal treatment and thermally treated. Therefore, these brush-painted aluminum plates show hydrophobic behavior, preventing water absorption at high relative humidity, which should be able to withstand weather conditions and the cycling of different conditions. The hydrophobicity, along with the thermal stability of these metal oxides, meets the requirements for selective coatings to be technologically viable as solar collector systems, ensuring durability during the operation processes and useful life.

**Figure 9.** Contact angle values for brush-painted aluminum plates using metal-oxide-based selective paints.

According to the results discussed, it seems that NiCo_2O_4 selective paint represents the best cost–benefit balance, considering the possibility of substituting a high content of cobalt with nickel, maintaining the spinel-type structure, enhancing thermal stability, and, most importantly, improving optical properties in comparison to pristine Co_3O_4 .

3.3. Scale-Up

Figure 10a shows the spray-painted aluminum fins using the NiCo_2O_4 -based selective paint that were used to assemble the flat solar collector manufactured by the Mexican company Módulo Solar S.A. de C.V. A representative reflectance spectrum of the spray-painted aluminum fins is shown in Figure 10b. Note that the aluminum fins used as substrates allowed the improvement of the surface to a mirror finish, favoring the balance between absorptance and thermal emittance. The difference observed in the reflectance spectra for the brush-painted aluminum plates (see Figure 8b) and spray-painted aluminum fins (see Figure 10b) for the NiCo_2O_4 selective paint can be related principally to the thickness obtained by using each procedure for coating preparation. In addition, it was observed that the optical properties of α and ϵ were better for the NiCo_2O_4 -based selective paint compared to the HVA commercial paint; see Table 5.

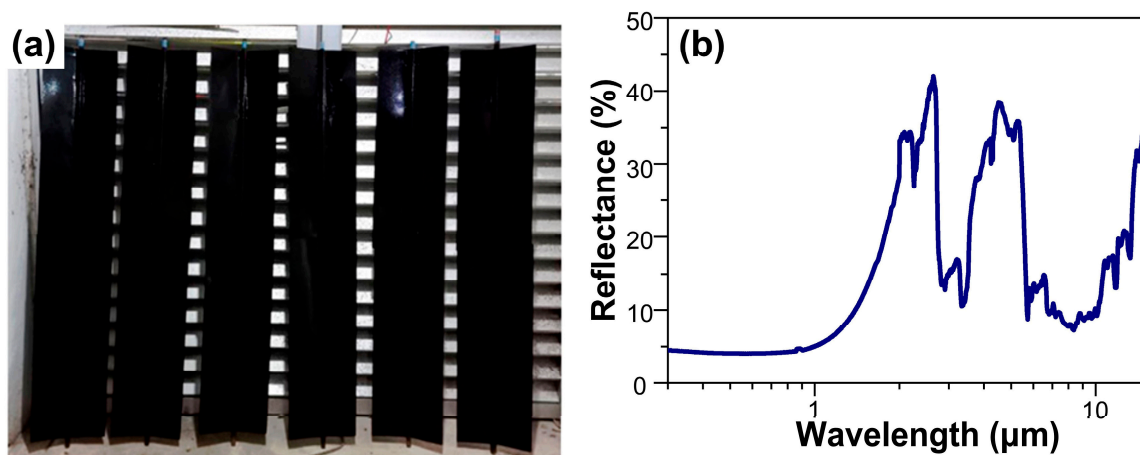


Figure 10. (a) Photograph of spray-painted aluminum fins (1.4 m × 0.8 m each) using NiCo₂O₄-based selective paint and thermally treated for 24 h at 200 °C and its (b) representative reflectance spectrum.

Table 5. Solar absorbance and thermal emittance values for spray-painted aluminum fins using NiCo₂O₄-based paint and HVA commercial paint used in the flat collector.

Sample	Spray-Painted without Thermal Treatment		Spray-Painted and Thermally Treated at 200 °C for 24 h	
	α (%)	ϵ (%)	α (%)	ϵ (%)
NiCo ₂ O ₄	96	69	95	67
HVA commercial	91	84	89	84

The spray-painted aluminum fins using the NiCo₂O₄-based selective paint were evaluated in a flat solar collector according to the NMX-ES-004-NORMEX-2010 Official Mexican Standard. Figure 11 shows a picture of the flat solar collector, and Table 6 contains the results of its thermal performance, which is characterized by its thermal efficiency (η), which represents the relationship between the useful energy transferred to the fluid (water) and the incident solar energy on the flat solar collector. Thermal efficiency can be calculated with the following equation:

$$\eta = mC_p(T_{out} - T_{in})/I \times A = Q/I \times A \quad (4)$$

where η is solar collector efficiency (%), m is the mass flow of water (g/s), C_p is the heat capacity of water (J/g °C), T_{out} is the outlet temperature (°C), T_{in} is the inlet temperature (°C), I is the solar irradiation (W/m²), A is the opening area (m²), and Q is the useful heat (J/s).

Table 6. Thermal performance obtained for flat solar collectors assembled with spray-painted aluminum fins using the NiCo₂O₄-based selective paint and the HVA commercial paint. The minimum limit values established by the Official Mexican Standard are also presented.

Solar Collectors	Useful Heat per 8 h Day (MJ)	Useful Heat per 24 h Day (MJ)	Useful Heat per Year in 8 h (MJ)	Useful Heat per Year in 24 h (MJ)
NiCo ₂ O ₄	12.6	9.0	4592	3280
HVA commercial	13.4	9.7	4890	3552
Minimum limit	12.5	8.7	4550	3170

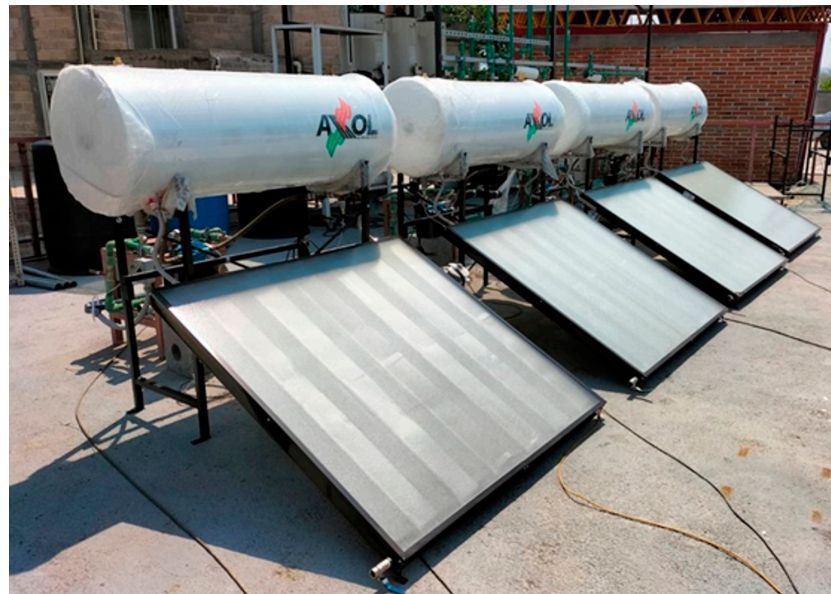


Figure 11. Photograph of the flat solar collectors assembled with spray-painted aluminum fins using the NiCo_2O_4 -based selective paint and other commercial paints for comparison purposes. Tests were evaluated according to the NMX-ES-004-NORMEX-2010 Official Mexican Standard.

The average thermal efficiency value oscillated between 46% and 50% for the flat solar collector assembled with the spray-painted aluminum fins using the NiCo_2O_4 -based selective paint. Hence, the useful heat generated by this collector can be an option to be tested in a complete collector for real applications, and it presents a thermal performance value above the Official Mexican Standard. Therefore, the formulated selective paint based on NiCo_2O_4 is an attractive option for other applications related to solar capturing. As presented in Table 6, the thermal performance of the NiCo_2O_4 -based selective paint was slightly lower compared to HVA commercial paint; however, our paint is competitive at present, and its performance can be optimized with a reformulation considering an active phase that allows reducing its emittance. Also, the use of fins with better roughness characteristics would help to improve efficiency.

4. Conclusions

Powders of nickel–cobalt mixed oxides were easily prepared using the simple nitrate decomposition reaction. The replacement of cobalt with nickel increased the cell parameter linearly and improved the redox capability through the presence of mixed valence states (2+ and 3+) both for nickel and cobalt. Powders and coatings (obtained with brush painting and spray painting) of nickel–cobalt mixed oxides presented similar optical properties to pristine Co_3O_4 , which means that cobalt can be substituted with nickel in a wide range of compositions (0.1 to 1), representing an important advantage in terms of cost and benefit toward its potential scale-up in solar technological applications because nickel nitrate is around three times cheaper than cobalt nitrate. The flat solar collector assembled with spray-painted aluminum fins using the NiCo_2O_4 -based selective paint showed an outstanding performance that competes well with a commercial collector, fulfilling the specifications according to the respective Official Mexican Standard. It was found that the spray-painted aluminum fins using the NiCo_2O_4 -based selective paint showed less emissivity at night, allowing more energy to be conserved in 24 h. The results presented in this paper show that solar absorber coatings prepared using selective paints of nickel–cobalt mixed spinel-type oxides offer great potential for application in large-scale solar collectors. However, there is an opportunity to improve the performance of both paints (reduce emittance) and coatings (use of fins with other geometry and surface roughness) to make nickel–cobalt oxides more attractive in terms of cost and benefit.

Supplementary Materials: The following supporting information can be downloaded at <https://www.mdpi.com/article/10.3390/coatings13081329/s1>: Figure S1. Photographs of all synthesized powders thermally treated at 500 °C; Figure S2. XRD powder pattern experimental (red), calculated (black) and profile fitting difference (blue) for the Le Bail refinement of the composition Co_3O_4 . Green bars correspond to Bragg positions; Figure S3. XRD powder pattern experimental (red), calculated (black) and profile fitting difference (blue) for the Le Bail refinement of the composition $\text{Ni}_{0.1}\text{Co}_{2.9}\text{O}_4$. Green bars correspond to Bragg positions; Figure S4. XRD powder pattern experimental (red), calculated (black) and profile fitting difference (blue) for the Le Bail refinement of the composition $\text{Ni}_{0.25}\text{Co}_{2.75}\text{O}_4$. Green bars correspond to Bragg positions; Figure S5. XRD powder pattern experimental (red), calculated (black) and profile fitting difference (blue) for the Le Bail refinement of the composition $\text{Ni}_{0.5}\text{Co}_{2.5}\text{O}_4$. Green bars correspond to Bragg positions; Figure S6. XRD powder pattern experimental (red), calculated (black) and profile fitting difference (blue) for the Rietveld refinement of the composition NiCo_2O_4 . Green bars correspond to Bragg positions. The determined phase percentage is 96.1 % for NiCo_2O_4 and 3.9 % for NiO; Figure S7. XRD powder pattern experimental (red), calculated (black) and profile fitting difference (blue) for the Rietveld refinement of the composition $\text{Ni}_{1.5}\text{Co}_{1.5}\text{O}_4$. Green bars correspond to Bragg positions. The determined phase percentage is 73.3 % for NiCo_2O_4 and 26.7 % for NiO; Figure S8. XRD powder pattern experimental (red), calculated (black) and profile fitting difference (blue) for the Le Bail refinement of the composition NiO. Green bars correspond to Bragg positions; Figure S9. Representative SEM-EDS mappings for all synthesized samples; Figure S10. Atomic percentage of surface oxygen obtained from XPS analysis for Co_3O_4 and $\text{Ni}_x\text{Co}_{3-x}\text{O}_4$ oxides; Figure S11. Representative SEM micrographs of selected samples: (a) $\text{Ni}_{0.1}\text{Co}_{2.9}\text{O}_4$, (b) $\text{Ni}_{0.5}\text{Co}_{2.5}\text{O}_4$, and (c) $\text{Ni}_{1.5}\text{Co}_{1.5}\text{O}_4$; Figure S12. Comparative weight variation obtained at 5 °C/min without dwell during three heating–cooling cycles for (a) Co_3O_4 and $\text{Ni}_x\text{Co}_{3-x}\text{O}_4$ with $x =$ (b) 0.1, (c) 0.25, (d) 0.5, (e) 1.0, and (f) 1.5; Figure S13. Reflectance spectra for polymeric resin on aluminum substrate: (a) as painted and (b) thermally treated at 200 °C for 24 h; Figure S14. Reflectance spectra for two sets of brush-painted aluminum plates using the commercial paint Solkote®: (a) without thermal treatment and (b) thermal treated at 200 °C for 24 h.

Author Contributions: Conceptualization, R.D.B.-M., D.M.H.-Z., G.R.-G. and M.Á.R.-G.; methodology, R.D.B.-M., D.M.H.-Z., G.R.-G. and M.Á.R.-G.; investigation, validation, and formal analysis, R.D.B.-M., D.M.H.-Z., M.Á.S., O.G.-V., A.P.F.-B., G.R.-G. and M.Á.R.-G.; resources, O.G.-V., G.R.-G. and M.Á.R.-G.; data curation, M.Á.S., R.D.B.-M., D.M.H.-Z., G.R.-G., and M.Á.R.-G.; writing—original draft preparation, writing—review and editing, M.Á.S., R.D.B.-M., D.M.H.-Z., G.R.-G. and M.Á.R.-G.; supervision, project administration, and funding acquisition, G.R.-G. and M.Á.R.-G. All authors have read and agreed to the published version of the manuscript.

Funding: This research was funded by Consejo Nacional de Ciencia y Tecnología, Grant Number C.B.-2015-255109; CONAHCYT, SENER, and IER-UNAM, Grant Number CeMIESol, Project P-81.

Institutional Review Board Statement: Not applicable.

Informed Consent Statement: Not applicable.

Data Availability Statement: No data were used for the research described in the article.

Acknowledgments: The authors gratefully acknowledge CONAHCYT for supporting R.D. Bacelis-Martínez through PhD scholarship 457777; M.A. Ruiz-Gómez through the projects Cátedra 1710 and C.B.-2015-255109; IER-UNAM, the postdoctoral scholarship program from UNAM-DGAPA; and funding through the Mexican Center for Innovation in Solar Energy (CeMIESol), Project P-81. The authors are grateful for using the LANNBIO Cinvestav-Mérida facilities, supported by the grants FOMIX Yucatán 2008–108160, CONACYT LAB-2009-01 123913, 292692, 188345, 204822, 292692, and 294643. The authors thank the Laboratorio Nacional de Conversión y Almacenamiento de Energía (LNCAE) for access to its experimental facility.

Conflicts of Interest: The authors declare no conflict of interest.

References

1. Rabaia, M.K.H.; Abdelkareem, M.A.; Sayed, E.T.; Elsaid, K.; Chae, K.J.; Wilberforce, T.; Olabi, A.G. Environmental Impacts of Solar Energy Systems: A Review. *Sci. Total Environ.* **2021**, *754*, 141989. [[CrossRef](#)]
2. Sharif, A.; Meo, M.S.; Chowdhury, M.A.F.; Sohag, K. Role of Solar Energy in Reducing Ecological Footprints: An Empirical Analysis. *J. Clean. Prod.* **2021**, *292*, 126028. [[CrossRef](#)]

3. Hosseini, S.E.; Wahid, M.A. Hydrogen from Solar Energy, a Clean Energy Carrier from a Sustainable Source of Energy. *Int. J. Energy Res.* **2020**, *44*, 4110–4131. [CrossRef]
4. Wu, Z.; Wang, J.; Liu, Y.; Hou, S.; Liu, X.; Zhang, Q.; Cao, F. A Review of Spectral Controlling for Renewable Energy Harvesting and Conserving. *Mater. Today Phys.* **2021**, *18*, 100388. [CrossRef]
5. Chen, X.; Zhang, D.; Wang, Y.; Ling, X.; Jin, X. The Role of Sensible Heat in a Concentrated Solar Power Plant with Thermochemical Energy Storage. *Energy Convers. Manag.* **2019**, *190*, 42–53. [CrossRef]
6. Gong, J.; Li, C.; Wasielewski, M.R. Advances in Solar Energy Conversion. *Chem. Soc. Rev.* **2019**, *48*, 1862–1864. [CrossRef]
7. Madhukeshwara, N.; Prakash, E.S. An Investigation on the Performance Characteristics of Solar Flat Plate Collector with Different Selective Surface Coatings. *Int. J. Energy Environ.* **2012**, *3*, 99–108. Available online: https://www.ijee.ieefoundation.org/vol3/issue1/IJEE_10_v3n1.pdf (accessed on 7 February 2022).
8. Zhang, J.; Wang, C.; Shi, J.; Wei, D.; Zhao, H.; Ma, C. Solar Selective Absorber for Emerging Sustainable Applications. *Adv. Energy Sustain. Res.* **2022**, *3*, 2100195. [CrossRef]
9. Sun, B.; Wang, L.; Sun, Y.; Ren, J.; Yang, Y.; Liu, H.; Liang, D.; Li, A.; Wang, C. Optical Performance, Thermal Stability, and Failure Analysis of the W_{N_x} - Si_3N_4 Multilayer Solar Selective Absorbing Coatings. *ACS Appl. Energy Mater.* **2022**, *5*, 1883–1893. [CrossRef]
10. Phani Kumar, K.K.; Mallick, S.; Sakthivel, S. Nanoparticles Based Single and Tandem Stable Solar Selective Absorber Coatings with Wide Angular Solar Absorptance. *Sol. Energy Mater. Sol. Cells* **2022**, *242*, 111758. [CrossRef]
11. Selikhov, Y.; Klemeš, J.J.; Kapustenko, P.O.; Arsenyeva, O. The Study of Flat Plate Solar Collector with Absorbing Elements from a Polymer Material. *Energy* **2022**, *256*, 124677. [CrossRef]
12. Liu, B.; Wang, C.; Bazri, S.; Badruddin, I.A.; Orooji, Y.; Saeidi, S.; Wongwises, S.; Mahian, O. Optical Properties and Thermal Stability Evaluation of Solar Absorbers Enhanced by Nanostructured Selective Coating Films. *Powder Technol.* **2021**, *377*, 939–957. [CrossRef]
13. Ma, P.; Geng, Q.; Liu, G. Photothermal Conversion Applications of the Transition Metal (Cu, Mn, Co, Cr, and Fe) Oxides with Spinel Structure. In *Magnetic Spinels—Synthesis, Properties and Applications*, 1st ed.; Seehra, M.S., Ed.; Intech Publisher: London, UK, 2017; Volume 12, pp. 273–284. [CrossRef]
14. Zaki, A.; Carrasco, J.; Bielsa, D.; Faik, A. Tunable Redox Temperature of a $Co_{3-x}Mn_xO_4$ ($0 \leq x \leq 3$) Continuous Solid Solution for Thermochemical Energy Storage. *ACS Appl. Mater. Interfaces* **2020**, *12*, 7010–7020. [CrossRef] [PubMed]
15. Ho, C.T.; Weng, T.H.; Wang, C.Y.; Yen, S.J.; Yew, T.R. Tunable Band Gaps of $Co_{3-x}Cu_xO_4$ Nanorods with Various Cu Doping Concentrations. *RSC Adv.* **2014**, *4*, 20053–20057. [CrossRef]
16. Krishnan, S.G.; Arulraj, A.; Khalid, M.; Reddy, M.V.; Jose, R. Energy Storage in Metal Cobaltite Electrodes: Opportunities & Challenges in Magnesium Cobalt Oxide. *Renew. Sustain. Energy Rev.* **2021**, *141*, 110798. [CrossRef]
17. Moore, R.J.; White, J. Equilibrium relationships in the system NiO-CoO-O₂. *J. Mater. Sci.* **1974**, *9*, 1393–1400. [CrossRef]
18. Han, L.; Meng, Q.; Wang, D.; Zhu, Y.; Wang, J.; Du, X.; Stach, E.A.; Xin, H.L. Interrogation of bimetallic particle oxidation in three dimensions at the nanoscale. *Nat. Commun.* **2016**, *7*, 13335. [CrossRef]
19. Nikolov, I.; Darkaoui, R.; Zhecheva, E.; Stoyanova, R.; Dimitrov, N.; Vitanov, T. Electrocatalytic activity of spinel related cobaltites $M_xCo_{3-x}O_4$ (M = Li, Ni, Cu) in the oxygen evolution reaction. *J. Electroanal. Chem.* **1997**, *429*, 157–168. [CrossRef]
20. Guan, X.; Luo, P.; Yu, Y.; Li, X.; Chen, D. Solvent-Tuned Synthesis of Mesoporous Nickel Cobaltite Nanostructures and Their Catalytic Properties. *Appl. Sci.* **2019**, *9*, 1100. [CrossRef]
21. Zhu, C.; Fu, S.; Du, D.; Lin, Y. Facilely Tuning Porous $NiCo_2O_4$ Nanosheets with Metal Valence-State Alteration and Abundant Oxygen Vacancies as Robust Electrocatalysts Towards Water Splitting. *Chem. Eur. J.* **2016**, *22*, 4000–4007. [CrossRef]
22. Eskandari, M.; Malekfar, R.; Buceta, D.; Taboada, P. $NiCo_2O_4$ -Based Nanostructured Composites for High-Performance Pseudocapacitor Electrodes. *Colloids Surf. A Physicochem. Eng. Asp.* **2020**, *584*, 124039. [CrossRef]
23. Li, Y.; Han, X.; Yi, T.F.; He, Y.; Li, X. Review and Prospect of $NiCo_2O_4$ -Based Composite Materials for Supercapacitor Electrodes. *J. Energy Chem.* **2019**, *31*, 54–78. [CrossRef]
24. Bacelis-Martínez, R.D.; Oskam, G.; Rodríguez Gattorno, G.; Ruiz-Gómez, M.A. Inkjet Printing as High-Throughput Technique for the Fabrication of $NiCo_2O_4$ Film. *Adv. Mater. Sci. Eng.* **2017**, *2017*, 9647458. [CrossRef]
25. Portilla-Nieto, Y.; Zaki, A.; Vidal, K.; Hernaiz, M.; Aranzabe, E.; Doppiu, S.; Faik, A. Development of $Co_{3-x}Ni_xO_4$ Materials for Thermochemical Energy Storage at Lower Red-Ox Temperature. *Sol. Energy Mater. Sol. Cells* **2021**, *230*, 111194. [CrossRef]
26. Shi, H.; Zhao, G. Water Oxidation on Spinel $NiCo_2O_4$ Nanoneedles Anode: Microstructures, Specific Surface Character, and the Enhanced Electrocatalytic Performance. *J. Phys. Chem. C* **2014**, *118*, 25939–25946. [CrossRef]
27. Macias, J.D.; Bacelis-Martínez, R.D.; Ruiz-Gómez, M.A.; Bante-Guerra, J.; Villafan-Vidales, H.I.; Rodríguez-Gattorno, G.; Romero-Paredes, H.; Alvarado-Gil, J.J. Thermophysical and Optical Properties of $NiCo_2O_4@ZrO_2$: A Potential Composite for Thermochemical Processes. *Int. J. Hydrogen Energy* **2021**, *46*, 10632–10641. [CrossRef]
28. Atchuta, S.R.; Sakthivel, S.; Barshilia, H.C. Nickel doped cobaltite spinel as a solar selective absorber coating for efficient photothermal conversion with a low thermal radiative loss at high operating temperatures. *Sol. Energy Mater. Sol. C* **2019**, *200*, 109917. [CrossRef]
29. Abidat, I.; Morais, C.; Comminges, C.; Canaff, C.; Rousseau, J.; Guignard, N.; Napporn, T.W.; Habrioux, A.; Kokoh, K.B. Three Dimensionally Ordered Mesoporous Hydroxylated $Ni_xCo_{3-x}O_4$ Spinel for the Oxygen Evolution Reaction: On the Hydroxyl-Induced Surface Restructuring Effect. *J. Mater. Chem. A* **2017**, *5*, 7173–7183. [CrossRef]

30. Yang, Z.; Tan, S.; Yang, J.; Li, Y.; Yang, X.; Deng, J. Study on the Solar Selectivity and Air Thermal Stability of Cobalt–Nickel–Iron Oxide Coating Fabricated by Spraying Method. *Opt. Mater.* **2021**, *111*, 110573. [[CrossRef](#)]
31. Rubin, E.B.; Chen, Y.; Chen, R. Optical Properties and Thermal Stability of Cu Spinel Oxide Nanoparticle Solar Absorber Coatings. *Sol. Energy Mater. Sol. Cells* **2019**, *195*, 81–88. [[CrossRef](#)]
32. Zäll, E.; Nordenström, A.; Järn, M.; Mossegård, J.; Wågberg, T. Environmentally Sustainable Electroplating of Selective Cobalt–Chromium Coating on Stainless Steel for Efficient Solar Collectors. *Sol. Energy Mater. Sol. Cells* **2022**, *245*, 111821. [[CrossRef](#)]
33. Herrera-Zamora, D.M.; Lizama-Tzec, F.I.; Santos-González, I.; Rodríguez-Carvajal, R.A.; García-Valladares, O.; Arés-Muzio, O.; Oskam, G. Electrodeposited Black Cobalt Selective Coatings for Application in Solar Thermal Collectors: Fabrication, Characterization, and Stability. *Sol. Energy* **2020**, *207*, 1132–1145. [[CrossRef](#)]
34. Geng, Q.; Zhao, X.; Gao, X.; Yu, H.; Yang, S.; Liu, G. Optimization Design of $\text{CuCr}_x\text{Mn}_{2-x}\text{O}_4$ -Based Paint Coatings Used for Solar Selective Applications. *Sol. Energy Mater. Sol. Cells* **2012**, *105*, 293–301. [[CrossRef](#)]
35. Kumar, K.K.P.; Mallick, S.; Sakthivel, S. Cobalt-Rich Spinel Oxide-Based Wide Angular Spectral Selective Absorber Coatings for Solar Thermal Conversion Applications. *Renew. Energy* **2023**, *203*, 334–344. [[CrossRef](#)]
36. Lizama-Tzec, F.I.; Herrera-Zamora, D.M.; Arés-Muzio, O.; Gómez-Espinoza, V.H.; Santos-González, I.; Cetina-Dorantes, M.; Vega-Poot, A.G.; García-Valladares, O.; Oskam, G. Electrodeposition of Selective Coatings Based on Black Nickel for Flat-Plate Solar Water Heaters. *Sol. Energy* **2019**, *194*, 302–310. [[CrossRef](#)]
37. Nunes, R.A.X.; Costa, V.C.; Sade, W.; Araújo, F.R.; Silva, G.M. Selective Surfaces of Black Chromium for Use in Solar Absorbers. *Mater. Res.* **2018**, *21*, e20170556. [[CrossRef](#)]
38. Kafle, B.P.; Basnet, B.; Timalisina, B.; Deo, A.; Malla, T.N.; Acharya, N.; Adhikari, A. Optical, Structural and Thermal Performances of Black Nickel Selective Coatings for Solar Thermal Collectors. *Sol. Energy* **2022**, *234*, 262–274. [[CrossRef](#)]
39. Khan, S.; Wu, Z.; ul haq, M.; Yuan, G.; Khan, M.; Song, C.; Han, G.; Liu, Y. Study of Annealing Effect Upon the Structural and Solar-Selective Properties of C/Ni/NiO Composite Coatings Prepared by Sol–Gel Method. *J. Sol-Gel Sci. Technol.* **2018**, *89*, 120–127. [[CrossRef](#)]
40. Kuboon, S.; Hu, Y.H. Study of NiO–CoO and Co_3O_4 – Ni_3O_4 Solid Solutions in Multiphase Ni–Co–O Systems. *Ind. Eng. Chem. Res.* **2011**, *50*, 2015–2020. [[CrossRef](#)]
41. Shannon, R.D.; Prewitt, C.T. Effective Ionic Radii in Oxides and Fluorides. *Acta Cryst.* **1969**, *B25*, 925–946. [[CrossRef](#)]
42. Le Bail, A.; Duroy, H.; Fourquet, J.L. Ab-initio structure determination of LiSbWO_6 by X-ray powder diffraction. *Mat. Res. Bull.* **1988**, *23*, 447–452. [[CrossRef](#)]
43. Rodríguez-Carvajal, J. *FullProf Suite*; Institute Leon Brillouin: Saclay, France, 2009.
44. Rashad, M.; Rüsing, M.; Berth, G.; Lischka, K.; Pawlis, A. CuO and Co_3O_4 Nanoparticles: Synthesis, Characterizations, and Raman Spectroscopy. *J. Nanomater.* **2013**, *2013*, 82. [[CrossRef](#)]
45. Hadjiev, V.G.; Iliev, M.N.; Vergilov, I.V. The Raman Spectra of Co_3O_4 . *J. Phys. C Solid State Phys.* **1988**, *21*, L199–L201. [[CrossRef](#)]
46. Sasmal, A.; Nayak, A.K. Morphology-Dependent Solvothermal Synthesis of Spinel NiCo_2O_4 Nanostructures for Enhanced Energy Storage Device Application. *J. Energy Storage* **2023**, *58*, 106342. [[CrossRef](#)]
47. Umeshbabu, E.; Rajeshkhanna, G.; Justin, P.; Rao, G.R. Magnetic, Optical and Electrocatalytic Properties of Urchin and Sheaf-Like NiCo_2O_4 Nanostructures. *Mater. Chem. Phys.* **2015**, *165*, 235–244. [[CrossRef](#)]
48. Gupta, J.; Ahmed, A.S. Interfacial Exchange Coupling and Defects Driven Magnetic and Optical Properties of Co_3O_4 -NiO Nanocomposites. *Phys. B* **2020**, *599*, 412383. [[CrossRef](#)]
49. Mironova-Ulmane, N.; Kuzmin, A.; Steins, I.; Grabis, J.; Sildos, I.; Pärs, M. Raman Scattering in Nanosized Nickel Oxide NiO. *J. Phys. Conf. Ser.* **2007**, *93*, 012039. [[CrossRef](#)]
50. Dupin, J.C.; Gonbeau, D.; Vinatier, P.; Levasseur, A. Systematic XPS Studies of Metal Oxides, Hydroxides and Peroxides. *Phys. Chem. Chem. Phys.* **2000**, *2*, 1319–1324. [[CrossRef](#)]
51. Carrillo, A.J.; Moya, J.; Bayón, A.; Jana, P.; de la Peña O’Shea, V.A.; Romero, M.; González-Aguilar, J.; Serrano, D.P.; Pizarro, P.; Coronado, J.M. Thermochemical Energy Storage at High Temperature Via Redox Cycles of Mn and Co Oxides: Pure Oxides Versus Mixed Ones. *Sol. Energy Mater. Sol. Cells* **2014**, *123*, 47–57. [[CrossRef](#)]
52. Tescari, S.; Agrafiotis, C.; Breuer, S.; de Oliveira, L.; Puttkamer, M.N.; Roeb, M.; Sattler, C. Thermochemical Solar Energy Storage Via Redox Oxides: Materials and Reactor/Heat Exchanger Concepts. *Energy Procedia* **2014**, *49*, 1034–1043. [[CrossRef](#)]
53. Agrafiotis, C.; Roeb, M.; Schmücker, M.; Sattler, C. Exploitation of Thermochemical Cycles Based on Solid Oxide Redox Systems for Thermochemical Storage of Solar Heat. Part 1: Testing of Cobalt Oxide-Based Powders. *Sol. Energy* **2014**, *102*, 189–211. [[CrossRef](#)]
54. Shi, X.; Bernasek, S.L.; Selloni, A. Formation, Electronic Structure, and Defects of Ni Substituted Spinel Cobalt Oxide: A DFT+U Study. *J. Phys. Chem. C* **2016**, *120*, 14892–14898. [[CrossRef](#)]
55. Ogawa, K.; Harada, J.; Fujiwara, T.; Takahashi, H. UV–vis Absorption Spectra of Powdered Materials: Direct Measurements by Optical Waveguide Spectroscopy. *Chem. Lett.* **2004**, *33*, 1446–1447. [[CrossRef](#)]
56. Mahavar, S.; Saquib Khan, M.; Yadav, T. Synthesis, Characterization and Testing of Black Metal Oxide Nanoparticles as Solar Concentrator Receiver Material. *Mater. Today-Proc.* **2019**, *8*, 22–27. [[CrossRef](#)]

57. Samos-Puerto, A.; Rodríguez-Gattorno, G.; Ruiz-Gómez, M.A. Fine tuning of inkjet printability parameters for NiO nanofilms fabrication. *Colloids Surf. A* **2019**, *583*, 123959. [[CrossRef](#)]
58. Hong, S.-J.; Mun, H.-J.; Kim, B.-J.; Kim, Y.-S. Characterization of Nickel Oxide Nanoparticles Synthesized under Low Temperature. *Micromachines* **2021**, *12*, 1168. [[CrossRef](#)]

Disclaimer/Publisher's Note: The statements, opinions and data contained in all publications are solely those of the individual author(s) and contributor(s) and not of MDPI and/or the editor(s). MDPI and/or the editor(s) disclaim responsibility for any injury to people or property resulting from any ideas, methods, instructions or products referred to in the content.